

Using Potential Field Extrapolations to Explore the Origin of Type II Spicules

VASYL YURCHYSHYN ¹, ANNELIESE SCHMIDT,² JIASHENG WANG ², XU YANG ¹,
EUN-KYUNG LIM ³ AND WENDA CAO ¹

¹*Big Bear Solar Observatory, New Jersey Institute of Technology,
40386 North Shore Lane, Big Bear City, CA 92314, USA*

²*New Jersey Institute of Technology,
Newark, NJ 07102, USA*

³*Korea Astronomy and Space Science Institute, Daedeokdae-ro 776, Yuseong-gu. Daejeon 34055,
Republic of Korea*

(Received June 20, 2023; Accepted Nov 15, 2023)

Submitted to *Astrophysical Journal*

ABSTRACT

We used 29 high resolution line of sight magnetograms (LOS) acquired with the Goode Solar Telescope (GST) in a quiet Sun area to extrapolate a series of potential field configurations and study their time variations. The study showed that there are regions that consistently exhibit changes in loop connectivity, whereas other vast areas do not show such changes. Analysis of topological features of the potential fields indicates that the photospheric footprint of the separatrix between open and closed loop systems well matches the roots of rapid blue and red shifted excursions (RBEs/RREs), which are disk counterparts of type II spicules. There is a tendency for the footpoints of the observed H_{α} features to be co-spatial with the footpoints of the loops that most frequently change their connectivity, while the area occupied by the open fields that did not show any significant and persistent connectivity changes is void of prominent jet and spicular activity. We also detected and tracked magnetic elements using the Southwest Automatic Magnetic Identification Suite and GST magnetograms, which allowed us to construct artificial magnetograms and calculate the corresponding potential field configurations. Analysis of the artificial data showed tendencies to those found for the observed data. The present study suggests that a significant amount of chromospheric activity observed in the far wings of the H_{α} spectral line may be generated by reconnecting closed loop systems and canopy fields consisting of “open” field lines.

Keywords: Sun: corona — Sun: flares — Sun: magnetic fields — Sun: activity

1. INTRODUCTION

Type II spicules (De Pontieu et al. 2007a) and their on-disk counterparts, identified as rapid blue or red-shifted excursions (RBEs/RREs, e.g., Rutten 2006; Langangen et al. 2008; Rouppe van der Voort et al. 2009; Sekse et al. 2013; Kuridze et al. 2015) have been the focus of many studies attempting to decipher their origin (e.g., De Pontieu et al. 2007b; McIntosh et al. 2011; De Pontieu et al. 2012; Tian et al. 2014; Pereira et al. 2014; Narang et al. 2016; Liu et al. 2019). Here, we use the term type II spicules, when referring to these events as a class, and we use the term RBE/RREs when referring to their H_α component observed on the disk.

Type II spicules are identified as short-lived (< 100 s), thin ($< 0''.7$), structures seen everywhere in *Hinode* Ca II images that show high Doppler velocities (50-150 km s⁻¹, De Pontieu et al. 2007a) and return flows (Pereira et al. 2014). Recently, Vilangot Nhalil et al. (2023) showed that H_α spectral lines of RBEs show i) broadening and increased line core absorption, ii) broadening and line core emission, and iii) broadening with absorption in the blue being stronger than in the red wing (see also Pereira et al. 2016; Bose et al. 2021).

When observed in IRIS data, they show higher apparent speeds of 80-300 km s⁻¹ (Tian et al. 2014; Narang et al. 2016). Type II spicules are omnipresent and carry a large amount of magnetic energy (De Pontieu et al. 2007b; McIntosh et al. 2011; De Pontieu et al. 2012; Liu et al. 2019). More details on the properties of RBEs / RREs may be found here (Yurchyshyn et al. 2020; Danilovic et al. 2023).

The source of RBEs/RREs is not well understood. Several theories have been proposed to explain their origin. One possibility is that p-mode waves leaking into the chromosphere create these plasma structures (e.g., Danilovic et al. 2023). Type II spicules have been observed to display twisting motions (e.g., Tomczyk et al. 2007; De Pontieu et al. 2012, 2014), doubling, and splitting (Suematsu et al. 2008; Yurchyshyn et al. 2020), and have been used as indicators of Alfvénic waves (De Pontieu et al. 2007b). Type II spicules and RBEs are subject to various high frequency oscillations (e.g., Okamoto & De Pontieu 2011; Sekse et al. 2013). Previously, De Pontieu et al. (2014) suggested that twisting motions could be the result of several processes such as strong photospheric vortical flows and the dissipation of torsional Alfvén waves they generate, the emergence of twisted flux tubes, the dissipation of torsional modes that arise from resonant absorption of swaying motions as well as magnetic reconnection (see also, Danilovic et al. 2023). Recently, Bose et al. (2023) argued that magnetic twist may propagate from a twisting spicule into coronal bright point associated loops and that spicules may be associated with heating to the transition region and coronal temperatures.

It is also possible that type II spicules are generated by the release of magnetic tension due to interactions between ions and neutrals or ambipolar diffusion (De Pontieu et al. 2017; Martínez-Sykora et al. 2017). This tension is introduced into the chromosphere when preexisting flux and new emerging flux interact, which suggests that these events should be closely linked to the emergence of new flux. Yurchyshyn et al. (2013) and Samanta et al. (2019) observed that some RBEs appeared in the Goode Solar Telescope (GST, Cao et al. 2010; Goode et al. 2010b,a) data shortly after opposite-polarity magnetic flux emerged near a cluster of dominant polarity.

There is also a growing body of evidence that type II spicules may be due to magnetic reconnection. Although is an attractive idea and Yurchyshyn et al. (2013) reported that some RBEs were of the inverted “Y” shape, due to the small size of the phenomena it is difficult to obtain direct evidence of reconnection driving RBE/RREs since not all events are associated with brightenings and/or inverted “Y” structures. Sterling et al. (2020) also advocated an idea that a microfilament eruption might be the fundamental driver of many spicules, especially those that are wide at the base, which again points toward magnetic reconnection as a key component of the process. Yurchyshyn et al. (2020) reported that RBEs evolve on time scales of several seconds and their evolution includes various patterns of rapid splitting of an RBE, or interaction of two or more closely situated RBEs. Deng et al. (2015) reported several examples where RBEs were possibly associated with flux emergence or cancellation events, while their analysis of 96 RBE events did not produce evidence of a statistical association between RBEs and flux emergence and cancellation. Taken together, these findings suggest that the origin of type II spicules might be related to the rearrangement of magnetic fields via magnetic reconnection caused by an emergence or cancellation event. In this case, a fraction of RBEs may originate due to the interchange reconnection driven by flux emergence and thus may be considered to be jets, while significant part of smaller and thinner events may be due to the so-called component reconnection, which occurs within a system of uni-directed and tangled field lines. Reconnection between a bundle of large-scale (or “open”) loops and emerging dipoles removes flux from the bundle, thus inducing their rapid equilibrium reconfiguration. The disturbance may also generate component reconnection and high-frequency MHD waves as proposed by van Ballegooijen et al. (2011), which, together with oscillatory reconnection (McLaughlin et al. 2012), may explain the appearance of smaller and thinner spicules II, as well as their group oscillations (McIntosh et al. 2011).

Here we further explore the possibility of reconnection being at the origin of RBEs/RREs. In this study we utilized an approach utilized by Cranmer & van Ballegooijen (2010), who used Monte Carlo method to generate a series of artificial quiet Sun “magnetograms” as a distribution of opposite polarity monopoles. These magnetograms were generated using a number of statistical rules of flux transport, emergence, and cancellations, which govern how magnetic elements evolve in the

photosphere. After that, potential fields were extrapolated in a 3D domain above each artificial magnetogram. The potential field lines were calculated and traced to identify which field lines “opened” or “closed” during a time step (see [Cranmer & van Ballegooijen 2010](#), for details). Here, we made use of this original idea with one substantial difference: the Monte Carlo simulated magnetograms were replaced with observed line-of-sight (LOS) magnetograms acquired with the Near Infra-red Imaging Spectropolarimeter (NIRIS, [Cao et al. 2012](#)). Comparison of extrapolation results based on a set of sequential LOS magnetograms allowed us to detect those locations where field lines change their connectivity due to new flux emergence, flows, and/or cancellation. In addition, we applied the Southwest Automatic Magnetic Identification Suite (SWAMIS, [DeForest et al. 2007](#)) to the NIRIS data set in order to detect and track magnetic elements. This information was used to construct a series of artificial magnetograms that were analyzed in the same manner as the observed data. In Section 2 we describe in detail the data preparation and the methods of analysis, while Section 3 presents results of the analysis. In Section 4 we summarize and discuss our findings.

2. DATA AND METHODS

The quiet Sun (QS) data were collected on 19 June 2017 in close proximity to the disk center at $(-60'', -40'')$ with the aid of an adaptive optics system. As mentioned above, RBEs and RREs display notable Doppler shift and line broadening and are best seen in the wings of the H_α line. Narrow band H_α images were acquired with the Visible Imaging Spectrometer (VIS), which utilizes a Fabry–Pérot interferometer with a bandpass of 0.008 nm and the possibility to shift the band-pass by 0.2 nm around the H_α line center. The pixel scale in this optical setup was $0''.029$ and the field of view (FOV) of the imager was $75'' \times 64''$. The observations were performed by rapidly switching between two spectral positions ($H_\alpha - 0.08$ and $H_\alpha + 0.08$ nm) with the resulting cadence of 3 s. The original data was acquired in bursts of 25 frames each and each burst was speckle reconstructed using the [Wöger & von der Lühe \(2007\)](#) speckle reconstruction technique to produce final images, which were aligned and de-stretched to remove residual image distortion induced by telescope jitters and seeing. The intensity of each image was adjusted to the average level of the data set. The comparison of two nearly co-temporal off-band images showed that the prominent dark structures present there are not co-spatial, indicating that these features are associated with asymmetrical line profiles, which is the main distinction of RBEs and RREs. The left and middle panels of [Figure 1](#) show averaged over 10 min interval $H_\alpha - 0.08$ nm and $H_\alpha + 0.08$ nm images. Averaging was performed to show the cumulative activity of RBEs and RREs in the FOV, thus highlighting the most active areas.

We used a set of 29 LOS magnetograms acquired between 18:37 UT and 19:22 UT ([Fig. 1](#), right) with NIRIS. The measurements were made using adaptive optics corrected light, a dual Fabry–Pérot etalon, and a $2K \times 2K$ HgCdTe Helium cooled

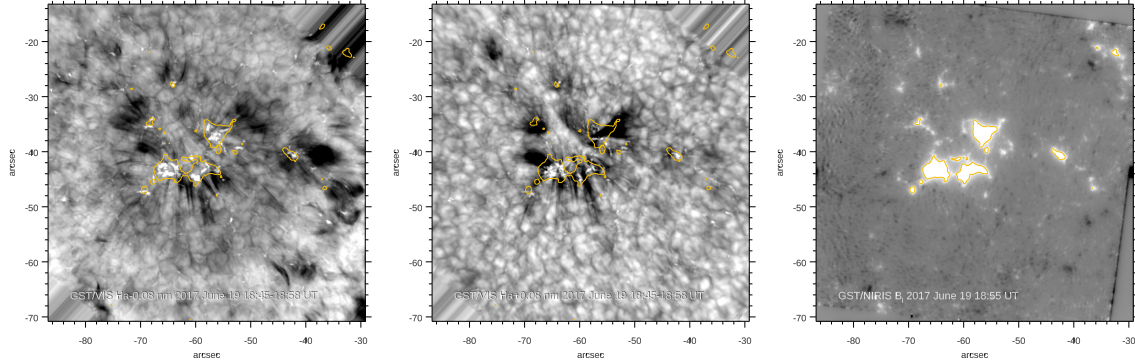


Figure 1. Left and center: averaged over a 10 min interval $H_{\alpha}-0.08$ nm and $H_{\alpha}+0.08$ nm images. Right: the corresponding GST/NIRIS B_l map saturated at ± 100 G level. The yellow contours in all panels are drawn at 100 G level.

Teledyne camera. Two polarization states are simultaneously imaged side-by-side on a 1024×1024 pixel area each, using a dual beam system that provides an $85''$ round FOV with image scale of $0''.08$ per pixel. The measurements were performed using the Fe I 1565 nm doublet with a bandpass of 0.01 nm and a rotating 0.35 wave plate that allows to sample 16 phase angles at each of more than 60 line positions at a cadence of 50 s per one full spectroscopic measurement (full-Stokes I, Q, U, V). The data set used in this study was corrected for polarization effects and calibrated using the weak field approximation. A co-temporal HMI SHARP (Scherrer et al. 2012; Schou et al. 2012; Bobra et al. 2014) data set was used to further calibrate the NIRIS data set.

The same VIS and NIRIS sets were used in a study of chromospheric spicules (Samanta et al. 2019) and small-scale magnetic elements (Abramenko & Yurchyshyn 2020). In particular, Abramenko & Yurchyshyn (2020) performed a detailed comparison of the NIRIS and HMI data and showed that on spatial scales below 3 Mm, the NIRIS instrument registered a larger amount of magnetic energy compared to HMI, although on large spatial scales, the ratio is reversed. These authors argued that this may be caused by differences in spatial resolution when large patches of HMI fields are observed with the NIRIS instrument as fragmented clusters consisting of several magnetic elements.

2.1. Potential Field Extrapolation

The potential field was computed using a method based on direct integration of the Green's function (Abramenko 1986; Metcalf et al. 2006), which is smoothed over each cell of a grid and analytically corrected for the influence of sampling. The computation is based on solving the Neumann boundary value problem for the Laplace equation, where the lower boundary condition is the vertical component of the magnetic field. Since the observed area was close to the disk center ($-60''$, $-40''$), it is safe to accept that the vertical B_Z component may be very well approximated by the observed LOS field, B_l .

The choice of the potential field extrapolation was based on the following considerations. At this moment, the potential field extrapolation is the only reasonable and widely available tool that can be applied to QS magnetic field measurements. Nonlinear extrapolation techniques require measurements of the vector field, which are unreliable over an extended QS area. A linear force-free technique can be used, however, applying a uniform alpha to a QS data will introduce a significant twist in many QS. The potential approach thus provides a ground truth that can be used to interpret the data. The studied FOV was dominated by a positive polarity flux and the magnetic field imbalance over the entire FOV is non-negligible, which influences the accuracy of the extrapolation results, especially so in case when the solution to the Laplace equation is expressed in terms of Fourier transforms of the boundary conditions. The numerical tool that we applied is based on direct integration of Green’s function, which is less susceptible to the flux imbalance (see, for example [Metcalf et al. 2006](#), page 270). One way to solve this imbalance problem is to pad the observed magnetogram with artificial small scale elements of negative polarity, or include an equally strong cluster of negative fields thus reducing the flux imbalance. Another way is to insert a NIRIS magnetogram into a large FOV HMI magnetogram. While it is possible, in reality it is a very difficult exercise since NIRIS data has to be smoothly integrated into HMI data, which is a difficult thing to do even for AR measurements, which have higher field strength. In order to include surrounding network fields, the width of the extrapolated FOV should at least triple or quadruple. Decreasing the resolution of the extrapolated data may mitigate the problem, but then we lose valuable information on the dynamics of small-scale magnetic fields. The FOV expansion will only affect the magnetic connectivity of the longest (“open”) field lines that leave the central area (as well as the short field lines at the edge which are not essential for the study). Further in the text we will show that a significant amount of the extrapolated magnetic flux does leave the computational domain though the upper boundary thus emulating the padding process. Finally, since the location of the main q-lane is determined by the lines that are fully rooted within the existing FOV, possible variations in the endpoints of the large-scale (“open”) field lines will not affect the result.

We applied the potential field extrapolation tool to each of the NIRIS magnetograms in the data series, which were pre-processed to minimize the influence of atmospheric distortions and noise of measurements. The original 720×720 pixel magnetograms with pixel size of $0''.08$ were re-scaled to a 360×360 grid with the new pixel size of $0''.16$. The height of the domain was $32''$ (200 pixels). First, the magnetic field images were de-stretched to remove residual image distortions and stabilize the position of magnetic elements within the FOV. Next, we filtered the data by applying a 3D 3-point moving average technique. This procedure resulted in removing and/or suppressing small scale rapidly fluctuating data points, while minimally affecting gradual large scale structures. Finally, we applied a step function $1/(1 + \exp(-0.05(|x| - 70)))$

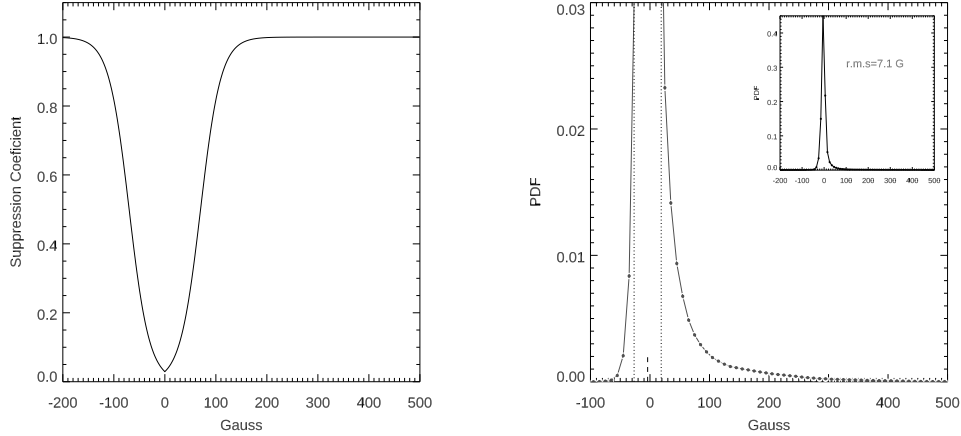


Figure 2. Left: Step function, $1/(1 + \exp(-0.05(|x| - 70)))$, used to filter the magnetic field data. Right: Normalized Probability Distribution Function of the B_l fields determined using a time sequence of 29 magnetograms. The inset shows the entire function, while the main panel zooms in on a fraction of the distribution. The short vertical dashed line at $x = -3.64$ indicated the mean, $\langle mean \rangle$, of the distribution, while the two dotted lines at $x = \langle mean \rangle \pm 21.3$ mark $\pm 3\sigma$ interval.

(Figure 2, left) to gradually suppress the strength of small-scale elements with peak intensities below 100 G. The step function lessened the contribution of noisy small scale elements and thus allowing us to generate relatively stable configurations with minimized influence of measurement noise.

The right panel in Figure 2 shows a probability distribution function (PDF) of the resulting B_l component derived from all 29 pre-processed magnetograms. The function is asymmetric, which reflects the fact that the scene is dominated by a large cluster of positive polarity fields surrounded by small scale and rather weak negative polarity elements. The mean calculated over all corrected magnetograms is very close to zero (2.5 G) and the r.m.s of the distribution is 7.1 G. While the main positive polarity patches, enclosed by contours in Figure 1 (right), appear unipolar without inclusions of opposite polarity fields, a multitude of small scale magnetic elements continuously emerged in close proximity to the contours as discussed by Samanta et al. (2019), (also see Fig. 4 in Abramenko & Yurchyshyn 2020). We note that the NIRIS sequence has a short data gap and its possible influence on the results will be discussed further in the text.

The purpose of this study is to explore how the magnetic configuration of a QS region is driven by the constantly evolving underlying magnetic fields. The study was inspired by the work of Cranmer & van Ballegooijen (2010) who performed quantitative energy estimates in the generated configurations, which is beyond the scope of the current study. Here we use observed NIRIS magnetograms for the same purpose. The preprocessing routine has significantly (and intentionally) affected the peak values of magnetic elements with initial intensities below 100 G, while the elements above that threshold were affected to a lesser degree. While we fully realize the limitations of the potential field approximation, we would like to note that we do not intend to

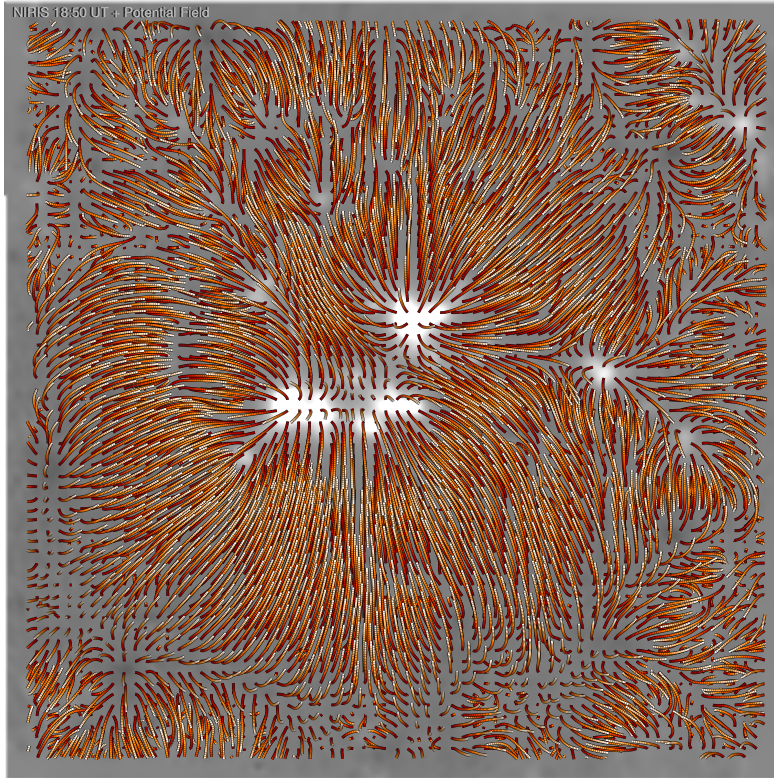


Figure 3. $3''.5$ long segments of potential field lines plotted over the 18:50 UT NIRIS magnetogram. The red endpoint of the field lines marks the beginning of a line and it is rooted in the photosphere.

reconstruct the realistic magnetic topology above the observed FOV but rather attempt to detect and visualize the most dynamic locations. On other hand, the spatial scales of the analysed structures are rather small ($< 10''$) and further in the text we will show that there is no drastic deviation between the observed H_α structures and extrapolated field lines.

3. RESULTS

In Figure 3 we plot potential field lines calculated using the 18:58 UT NIRIS B_l magnetogram. The field configuration is similar to what is expected to be observed in a QS region: the outskirts of the cluster region (network fields) are associated with closed loops of various lengths with their remote footpoints rooted at the numerous small-scale elements (internetwork fields), while the central part of the cluster is associated with open field lines that rapidly expand, creating a canopy above the loops. Note that to keep this plot readable we plotted only $3''.5$ long “legs” of the field lines with the dark red endpoint being “rooted” in the photosphere.

We calculated field lines for each magnetogram in the set on a fixed 72×72 grid, i.e., with a $0''.8$ step. We then analyzed the lines assigning the following attributes: “open” and “closed”. An “open” field line is defined as a line that leaves the domain thru the upper boundary. Next, using two closest sequential extrapolations, we determined the status of each line, i.e., whether a given line became i) opened, ii) closed, iii) changed

the position of its remote endpoint by more than $3''.2$ (4 nodes), or iv) remained unchanged. The $3''.2$ threshold was chosen because it is comparable to the size of a granule (see, for example, the middle panel in Figure 1). Therefore, the “relocation” of the endpoint by more than $3''.2$, indicates that the line may have jumped from one magnetic element to another as opposed to simply wandering within the same element. Hereinafter, we will refer to these lines as “jumped”. This comparison was made for 28 pairs of sequential magnetograms. We built 2D masks that contain information on coordinates of the pixels where the field lines changes occurred, type of changes, as well as the number of occurrences at a given pixel. In general, the majority of pixels in the 72×72 grid were associated with a changing line, however, many of the pixels displayed repeated status changes. In the upper left panel of Figure 4 we show a cumulative plot (top view) of all lines selected from all extrapolation sets that originated at pixels showing a large number of changes. In particular, we selected only those pixels, where field lines closed more than 7 times (green), which is about 75th percentile of the maximum detected loop closing events. Similarly, we plot “jumped” field lines (purple) at the pixels where the change occurred more than 15 times, which is as well 75th percentile of the maximum number of events. Since the number of lines that opened was much smaller here, we plot all lines that “opened” at a given pixel at least two times (red). As we noted earlier, there was a 12 min data gap in the NIRIS sequence, which caused nearly all of the field lines to change their connectivity. However, because we discard all connectivity changes that occurred only once at a given pixel, this data gap did not affect the results.

In the upper right panel of Figure 4 we show another projection of the same lines, while some short lines at the edges of the FOV were removed for clarity. There, to fully visualize the configuration, we also added open field lines (blue) that did not show any status change described above. The blue lines rapidly expand with height, forming a canopy above the closed loops. To mimic the observed small-scale chromospheric jet and spicules, in the lower left panel we plot only $5''$ long “legs” of the field lines shown in the upper left panel, while the lower right image is a pseudo-Doppler map constructed by subtracting the average $H_\alpha-0.08$ nm image (Figure 1, left) from the average $H_\alpha+0.08$ nm image (Figure 1, middle). [Samanta et al. \(2019\)](#) used the same data set and in their Figure 4 authors overplot co-temporal AIA 17.1 nm and VIS $H_\alpha-0.08$ nm images. The most prominent AIA 17.1 nm features appear to be well aligned with the underlying H_α spicules. There are no large-scale AIA 171.1 nm loops rooted at the center of the cluster that could be used to trace a magnetic connection between the magnetic area under study and the surrounding network fields. Comparison of the lines shown in Figure 4, c and H_α images shown in Figures 1, 4c and 5b indicated that the orientation of the observed H_α features agrees rather well with the plotted potential field line segments.

As we can see from the line plots, persistent changes in the magnetic configuration did not occur uniformly over the field of view. Moreover, there are several encouraging

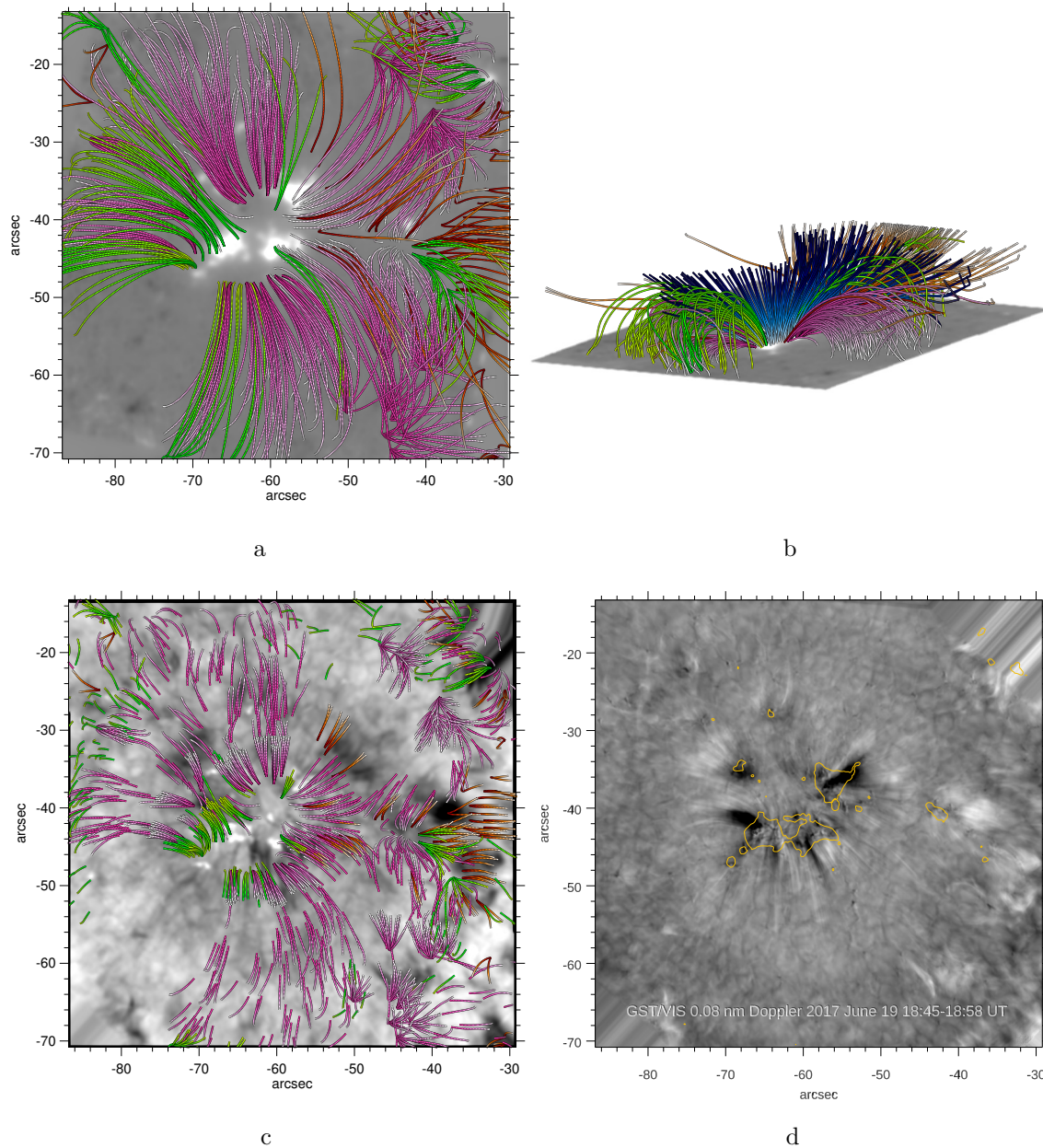


Figure 4. Potential field lines plotted over a NIRIS B_l magnetogram (a, b), and the averaged H_α -0.08 nm image (c). To ease the comparison, in panel d we plot a 100 G B_l contour (yellow) over a pseudo-Doppler image generated from the averaged H_α -0.08 nm and H_α +0.08 nm images presented in Fig. 1. The white/black patches indicate blue/red shifts. The field line color coding is the following: red - lines that opened; green - lines that closed; purple - lines that changed their endpoint; and blue - unchanged open lines. To avoid overcrowding, panel b shows only a fraction of the lines plotted in panel a and the vantage point is located in the lower left of panel a. Panel c shows only short, $3''.5$ long segments of the loops plotted in panel a. The field of view shown in these panels is the same as in Fig. 1.

moments: i) the lower left corner of the line plots is nearly void of the field lines which agrees with the observed lack of H_α activity in this area, ii) orientation and location of the majority of the observed H_α features coincide with those of the detected loops, and iii) the area occupied by the unchanged (blue) open field lines is nearly void of significant jet and spicular activity. These indicate that the utilized approach may indeed be useful for understanding the nature of these events.

The two data sets used in the study were acquired with a substantially different cadence, 3 s for H_α images versus 50 s for magnetograms. It has been shown earlier (e.g., Sekse et al. 2013; Yurchyshyn et al. 2020) that RBEs have a very short lifespan of 1 min or less and evolve on time scales of order of 1 s, so that the 3 s cadence seems adequate for detecting all events with lifetimes exceeding 3 s. On the other hand, the magnetic fields evolve on somewhat longer time scales comparable with the average lifetime of solar granulation (e.g., 8.6 min, Bahng & Schwarzschild 1961). More recent estimates based on Sunrise 33 s cadence data suggest that the median lifetime of weaker internetwork magnetic elements is 66 s Anusha et al. (2017). It appears that the NIRIS data acquired with the state-of-the-art 50 s cadence is adequate to detect and track the majority of small-scale elements with lifetimes exceeding 1 min, which constitutes the majority of detectable magnetic elements.

To further explore the derived magnetic configuration, we employed the technique of mapping the squash factor, q , previously developed by Titov et al. (2002), Titov (2007) and Liu et al. (2016). In Figure 5 (left) we show a typical $\log q$ (hereinafter q) map calculated from the 18:59 UT extrapolated set. The image represents a mixture of high intensity lanes of various widths, smoothly varying q parameters, and q “bubbles” surrounded by high intensity q -lanes. The blue and red shades indicate underlying polarity of line-of-sight magnetic fields, while the yellow and green areas indicate patches with open field lines. These q -lanes represent the photospheric footprint of separatrix or quasi-separatrix layers (QSL, e.g., Demoulin et al. 1996), where the mapping of field lines is discontinuous or there is a drastic change in field-line linkage. Thus, magnetic field lines that originate at the opposite sides of a q -lane do not belong to the same flux system and their endpoints are well separated. The q “bubbles”, which are the small features that include a blue patch and are outlined by a strong (red) q lane, represent a bipolar magnetic domain associated with a parasitic (positive, blue in this case) polarity surrounded by the main (red) polarity.

The red contour in the left panel highlights a major q -lane that is the boundary between two large-scale q -features: the blue shaded area that indicates the footprints rooted in the positive polarity flux and the light green area that includes footprints of open field lines. The same contour is plotted over the average H_α -0.08 nm image (Figure 5, right) to highlight that the majority of dynamic H_α events are rooted in or close to the red contours. This, in turn, indicates that these events may have a spatial correlation with the QSL that separates systems of closed and open loops,

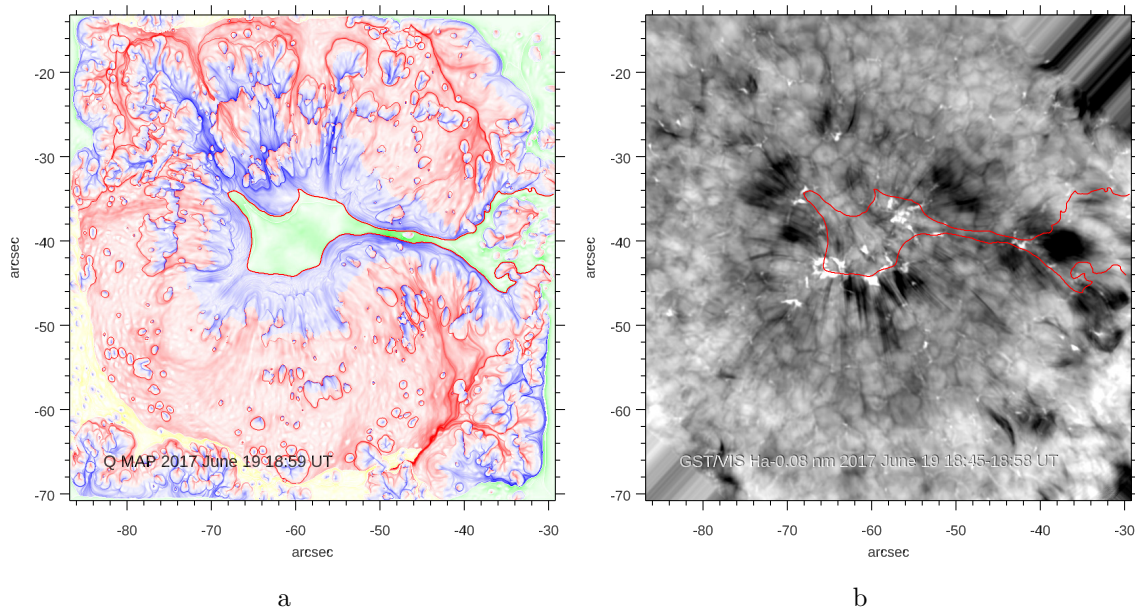


Figure 5. Left: a q-map calculated from the 18:59 UT extrapolated set. The blue and red shades indicate underlying polarity of line-of-sight magnetic fields, while the yellow and green areas indicate patches with open field lines. The red contour highlights the boundary between open and closed field lines. Right: the average H α -0.08 nm image (the same as in Fig. 1) with a red contour that is the same as in the left panel.

which leads us to suggest that magnetic reconnection may play a role in the origin of RBE/RREs.

There are other extended areas of “open” flux, represented in the left panel of Fig. 5 with long and wide yellow and green lanes running parallel and close to the boundary of the FOV. These “open” flux lanes are associated with magnetic fields leaving the domain via vertical and horizontal boundaries and most likely their presence and shape are strongly influenced by the finite size of the extrapolation domain. For that reason we do attempt to draw a comparison between the magnetic structures and chromospheric dynamics in these areas.

3.1. Modeling of Loop Dynamics Using Artificial Magnetograms

To exclude the possibility that the residual background noise in NIRIS magnetograms caused the observed changes in line connectivity, we constructed a series of artificial magnetograms based on the NIRIS set. We used SWAMIS tool to detect and track all NIRIS elements with $B_l \geq 90$ G. This threshold was defined in part by the above mentioned step function (Fig 2, left) and the fact that many ≤ 90 G elements resulted from varying seeing conditions at the edge of the FOV, which were not satisfactory corrected by the AO system.

The implementation of SWAMIS is primarily designed for identifying the magnetic features and characterizing field behavior at the photosphere, such as the size, vertical flux, and lifetime of individual magnetic features. Following the pre-processing routine in Section 2.1, the magnetograms were further filtered to remove p -mode oscillation

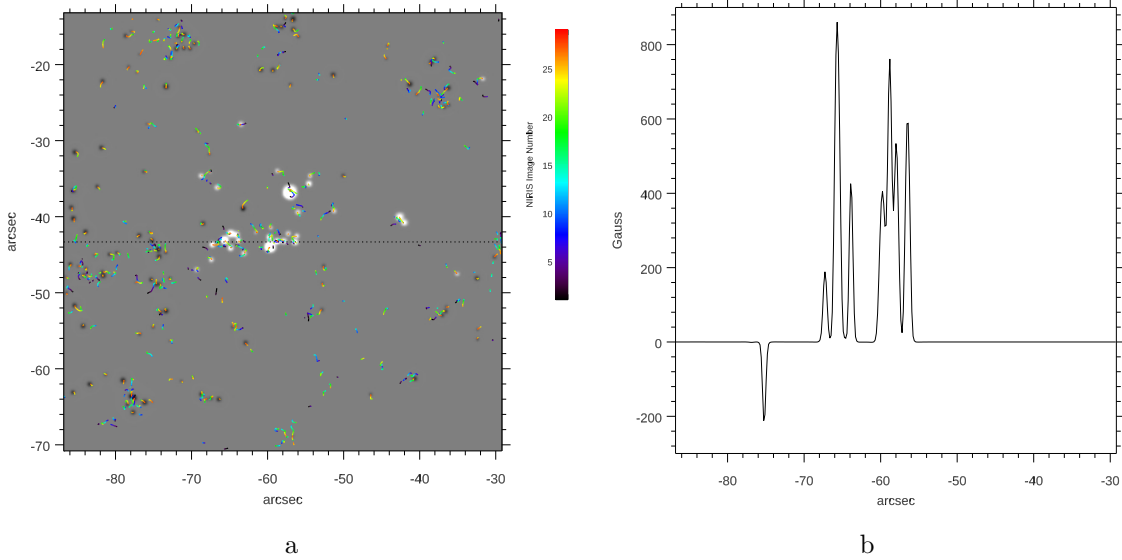


Figure 6. Left: Generated B_z map overplotted with tracks of magnetic elements. The color coding indicates in which frame a given element appeared and disappeared. The white/black patches indicate positive/negative polarity. The horizontal dotted line indicates the position of the B_z profile plotted in the right image.

and granulation noise. Since SWAMIS uses hysteresis that requires two (low/high) thresholds to reduce false positive detection, 3σ and 6σ of the Gaussian fit profile in 29 preprocessed magnetograms were used to discriminate magnetic elements above noise level. Only the detected pixels that survive in more than three consecutive frames were identified as magnetic elements. By setting the smallest maximum feature size in its lifetime to 4×4 pixels (0.11 arcsec^2), the minimal flux detection of weak features is $0.53 \times 10^{17} \text{ Mx}$. The locations of the detected features are defined by finding flux-weighted average pixel indices ($\sum_i^n B_l x_i / \Phi$ and $\sum_i^n B_l y_i / \Phi$, with Φ being the total flux).

Using SWAMIS output, we constructed 29 artificial (SWAMIS) magnetograms in the following way. Since the SWAMIS algorithm performed a tracking of all detected elements, we first smoothed the flux time profile of each element to minimize flux fluctuations. Then, for each SWAMIS element detected in each NIRIS frame, we generated a circular “monopole” using a Gaussian function with the total flux and area equal to those of the detected SWAMIS element. The peak of the Gaussian function was set to be three times of the averaged flux in the SWAMIS element. The generated element was then placed at the location provided by the SWAMIS algorithm. All unoccupied pixels were set to zero. Figure 8 (left) shows an example of the generated magnetogram with overplotted tracks for each element. The color legend indicates frames in which the element was first detected and disappeared. As can be seen in the graph, the largest detected displacement was about $2''$. The right panel in Figure 8 plots values along a row of the artificial magnetogram that crosses

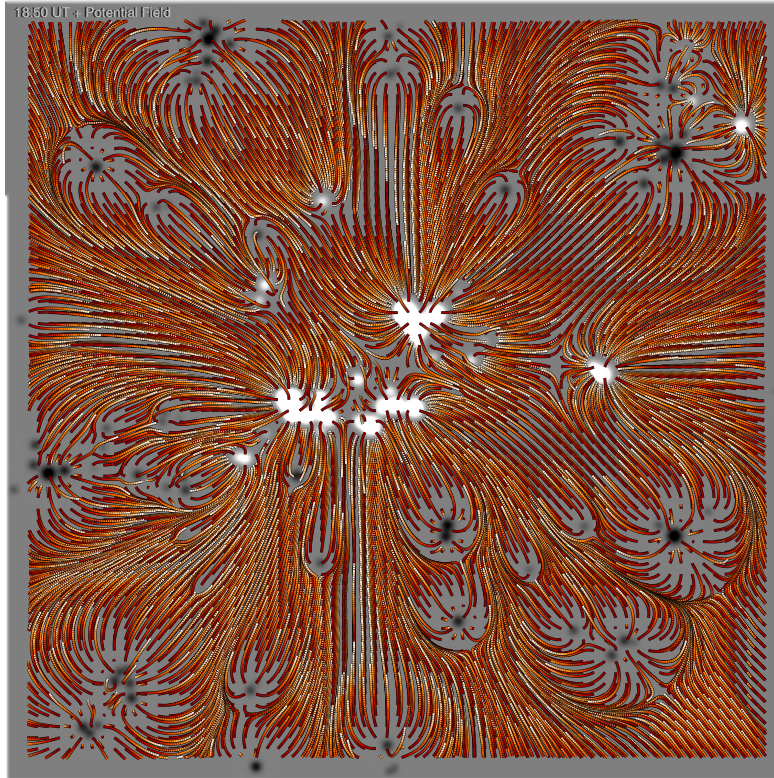


Figure 7. Potential field lines plotted over the 18:50 UT SWAMIS generated magnetogram. Only shorter field lines are plotted to highlight the magnetic connection between the elements, while larger field lines were not included.

the center of the FOV (indicated by the dotted line). Because the SWAMIS shapes were converted to circular, some elements are overlapping, which creates a profile somewhat resembling those that can be derived from an observed magnetogram. We then calculated the corresponding potential fields and analyzed their changes in the same manner we did for the observed data. We should note that the experiment with this toy model based on SWAMIS data is not intended to model the observed data, but is rather intended for better understanding of what drives the changes in magnetic field connectivity.

Figure 7 shows an example of the obtained potential field configuration. This line plot appears a bit different from a typical line plot (e.g., Figure 4, a) in a way that it highlights different flux domains and connections between magnetic elements. As expected, most of the small peripheral elements are connected to the central cluster of large positive polarity elements. This plot also visualizes the sensitive balance that exists in a magnetic configuration. Generally speaking, changes in the magnetic flux (emergence or submergence) and position of magnetic elements will cause changes in the volume of the corresponding domains, which inevitably will result in magnetic field lines to changing their connectivity. The most intense and persistent changes will occur at the boundary of two (or more) interacting flux systems, which may explain RBEs and RREs occurring in localized series.

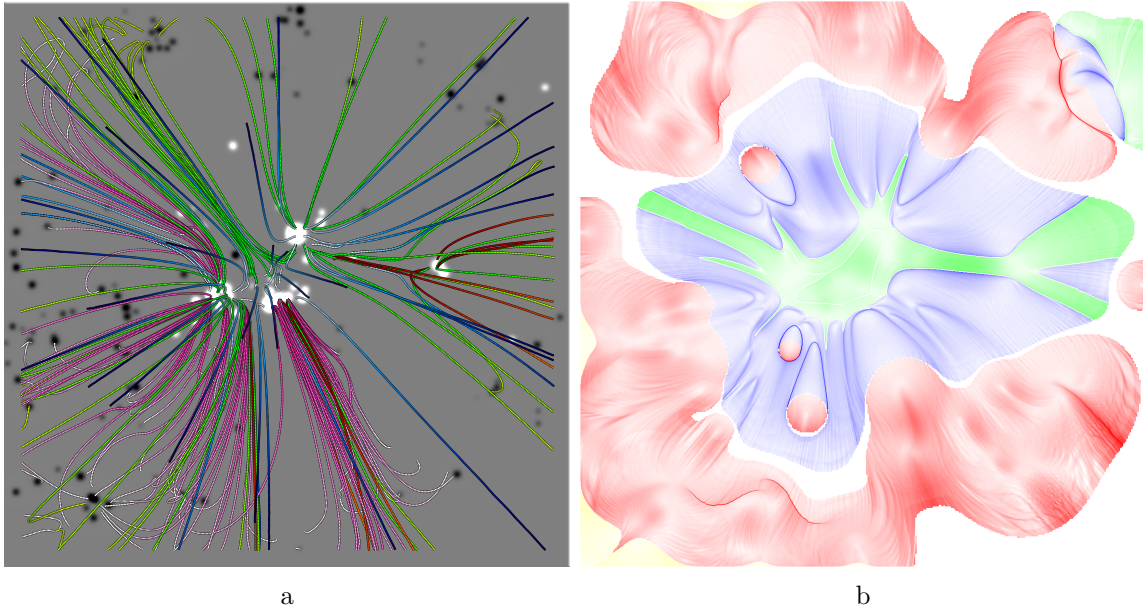


Figure 8. Left: Potential field lines plotted over an artificial magnetogram generated from SWAMIS data. The field line color coding is the following: red - lines that opened; green - lines that closed; purple - lines that changed their endpoint; and blue - unchanged open lines. Right: a q -map calculated from a set of potential field extrapolations based on the artificial magnetogram shown in the left panel. The blue and red shades indicate underlying polarity of line-of-sight magnetic fields, while green areas indicate patches with open field lines.

Following the approach used for NIRIS extrapolations, in Figure 8 (left) we plot opened, closed and changed field lines. Although the overall pattern differs from the NIRIS result (e.g., the lower left corner in the left panel of Figure 8 displays higher “activity” compared to that in Figure 4) the same tendency is observed for selected locations to be associated with repeated variations in line connectivity. The right panel in Figure 7 is the corresponding q -map, which shows similarities with the q -map in Figure 5 on large scales, however, details differ. In both cases open field lines dominate the center of the image (green) and this area is surrounded by closed loops. In both maps, there is a narrow lane of open field lines that runs from the center of the FOV to the right side of the FOV.

4. SUMMARY AND DISCUSSION

In summary, analysis of a series of LOS magnetograms and potential field extrapolations showed that there are regions that consistently exhibit changes in loop connectivity, while other vast areas do not show such changes. Analysis of topological features of a potential configuration calculated for a quiet Sun area indicates that the photospheric footprint of the separatrix between open and closed loop systems well matches the roots of RBEs/RREs. In particular, we would like to highlight that i) the footpoints of the observed H_{α} features coincide with the footpoints of the detected

loops, and ii) the area occupied by the open fields that did not show any significant and persistent connectivity changes is also void of prominent jet and spicular activity.

Another inference is that many locations of enhanced and persistent H_α activity are mainly associated with closed or opened field lines. [Samanta et al. \(2019\)](#) performed detailed comparison of jetting and magnetic activity using the same data set and reported that some of the observed jets were co-spatial and co-temporal with flux emergence or cancellation. Using another NIRIS data set [Yurchyshyn et al. \(2013\)](#) reported that a series of RBE events were temporally and spatially correlated with the appearance of new, mixed, or unipolar fields in close proximity to the network field, although a one-to-one correlation between an emergence event and an RBE/RRE event was not frequently detected. A single cancellation or reconnection event may cause re-configuration of a stable magnetic system thus triggering a chain of small-scale reconnection events that might give rise to a series of RBEs. The potential field approach that we applied here seems to be in line with these two earlier reports.

[Yurchyshyn et al. \(2013\)](#) also noted that RBEs show a tendency to occur at the interface between large-scale magnetic fields and small-scale dynamic magnetic loops, suggesting that RBEs are likely to be associated with the existence of a magnetic canopy. This suggestion is further supported here by the fact that footpoints of the observed jets tend to be located at, or in close vicinity of, the long and intense q -lane that separates closed loops systems and overlying canopy fields. The field lines located near a separatrix layer, dividing the open and closed systems, are subjected to rapid and frequent variations as the two systems evolve (see, for example, [Mason et al. 2023](#)). Recently, [Wang et al. \(2022\)](#) noted that spicular activity near the boundary of a coronal hole was associated with numerous flux cancellation events occurring at the edges of the main cluster of the magnetic field. Flux emergence or cancellation in close proximity to a q -lane may lead to multiple reconnection events driving RBEs and disturb the existing interface between the two flux systems, resulting in the occurrence of a series of multiple faint RBE events.

The “ q -bubbles” that we mentioned earlier, occur when a small bipole emerges within a unipolar field far away from a main cluster of magnetic fields (network fields). Thus, interchange reconnection may occur at the remote endpoint of a closed loop, associated with such as “bubble”, which will cause the footpoint to jump to another close location. [Yurchyshyn et al. \(2020\)](#) described short-lived, faint, and rapidly splitting RBEs that were hypothesized to result from reconnection within intertwined and tangled magnetic fields. [Wang et al. \(2022\)](#) concluded that disappearance of magnetic elements is realized through cancellation, fragmentation of unipolar clusters, or merging with elements of the same polarity. These activities at the remote footpoint may also contribute to the disturbance of the open-closed flux interface and trigger small-scale reconnections within flux systems that would manifest themselves as less intense, fast-varying splitting features.

An alternative interpretation of the spatial correspondence between the q-structures and chromospheric activity may be based on the 2.5D MHD simulation by [Martínez-Sykora et al. \(2017, 2018\)](#). These results suggest that magnetic tension, injected in the solar atmosphere by small-scale emerging fields may be rapidly released in the upper chromosphere thus driving strong upflows with parameters consistent with those measured for type II spicules. These weak emerging fields result from shredding of strong fields by convective motions. Authors argue that necessary conditions are typical for QS areas dominated by vertical magnetic flux concentrations of several kilogauss, such as the magnetic cluster analyzed in the present study. It is therefore likely that the mechanism proposed in [Martínez-Sykora et al. \(2017\)](#) may play a role in generating the RBEs and RREs discussed here. It is also possible that both reconnection and tension release mechanisms may operate alongside each other producing similar RBE type features. [Bose et al. \(2021\)](#) showed that RBEs can display different spectral profiles including various combinations of broadening, wing absorption, and Doppler offsets. It is therefore likely that these differences in spectral profiles may be unique footprints of different generation mechanisms at work.

Finally, we would like to emphasize that the present study is not aimed at proving the reconnecting nature of RBEs/RREs and neither it is designed to reconstruct realistic magnetic field configurations associated with network fields. Instead, we used observed data to explore possible dynamics in magnetic structures that likely exist in QS areas and to show that conditions, necessary for sustained generation of RBEs/RREs, may exist in the vicinity of a cluster of magnetic fields.

ACKNOWLEDGMENTS

We thank anonymous referee for constructive criticism and suggestions led to improvement of the paper. BBSO operation is supported by US NSF AGS 2309939 and 1821294 grants and New Jersey Institute of Technology. The GST operation is partly supported by the Korea Astronomy and Space Science Institute and the Seoul National University. V.Y. acknowledges support from NASA 80NSSC20K0025, 80NSSC20K1282, and 80NSSC21K1671 grants, and NSF AGS 2309939, 2300341, and AST 2108235, 2114201 grants. A.S. acknowledges support from NJIT's Undergraduate Research and Innovation (URI) Program, as well as NSF AGS-1954737 grant.

Facilities: GST

REFERENCES

- | | |
|----------------------------------|--|
| Abramenko, V. I. 1986, Byulletin | Abramenko, V. I., & Yurchyshyn, V. B. |
| Solnechnye Dannye Akademii Nauk | 2020, MNRAS, 497, 5405, |
| SSSR, 8, 83 | doi: 10.1093/mnras/staa2427 |

- Anusha, L. S., Solanki, S. K., Hirzberger, J., & Feller, A. 2017, *A&A*, 598, A47, doi: [10.1051/0004-6361/201527738](https://doi.org/10.1051/0004-6361/201527738)
- Bahng, J., & Schwarzschild, M. 1961, *ApJ*, 134, 312, doi: [10.1086/147160](https://doi.org/10.1086/147160)
- Bobra, M. G., Sun, X., Hoeksema, J. T., et al. 2014, *SoPh*, 289, 3549, doi: [10.1007/s11207-014-0529-3](https://doi.org/10.1007/s11207-014-0529-3)
- Bose, S., Joshi, J., Henriques, V. M. J., & Rouppe van der Voort, L. 2021, *A&A*, 647, A147, doi: [10.1051/0004-6361/202040014](https://doi.org/10.1051/0004-6361/202040014)
- Bose, S., Nóbrega-Siverio, D., De Pontieu, B., & Rouppe van der Voort, L. 2023, *ApJ*, 944, 171, doi: [10.3847/1538-4357/acb544](https://doi.org/10.3847/1538-4357/acb544)
- Cao, W., Goode, P. R., Ahn, K., et al. 2012, in *Astronomical Society of the Pacific Conference Series*, Vol. 463, Second ATST-EAST Meeting: Magnetic Fields from the Photosphere to the Corona., ed. T. R. Rimmele, A. Tritschler, F. Wöger, M. Collados Vera, H. Socas-Navarro, R. Schlichenmaier, M. Carlsson, T. Berger, A. Cadavid, P. R. Gilbert, P. R. Goode, & M. Knölker, 291
- Cao, W., Gorceix, N., Coulter, R., et al. 2010, *Astronomische Nachrichten*, 331, 636, doi: [10.1002/asna.201011390](https://doi.org/10.1002/asna.201011390)
- Cranmer, S. R., & van Ballegoijen, A. A. 2010, *ApJ*, 720, 824, doi: [10.1088/0004-637X/720/1/824](https://doi.org/10.1088/0004-637X/720/1/824)
- Danilovic, S., Bjørgen, J. P., Leenaarts, J., & Rempel, M. 2023, *A&A*, 670, A50, doi: [10.1051/0004-6361/202244466](https://doi.org/10.1051/0004-6361/202244466)
- De Pontieu, B., Carlsson, M., Rouppe van der Voort, L. H. M., et al. 2012, *ApJL*, 752, L12, doi: [10.1088/2041-8205/752/1/L12](https://doi.org/10.1088/2041-8205/752/1/L12)
- De Pontieu, B., Martínez-Sykora, J., & Chintzoglou, G. 2017, *ApJL*, 849, L7, doi: [10.3847/2041-8213/aa9272](https://doi.org/10.3847/2041-8213/aa9272)
- De Pontieu, B., McIntosh, S., Hansteen, V. H., et al. 2007a, *PASJ*, 59, 655. <https://arxiv.org/abs/0710.2934>
- De Pontieu, B., McIntosh, S. W., Carlsson, M., et al. 2007b, *Science*, 318, 1574, doi: [10.1126/science.1151747](https://doi.org/10.1126/science.1151747)
- De Pontieu, B., Rouppe van der Voort, L., McIntosh, S. W., et al. 2014, *Science*, 346, 1255732, doi: [10.1126/science.1255732](https://doi.org/10.1126/science.1255732)
- DeForest, C. E., Hagenaar, H. J., Lamb, D. A., Parnell, C. E., & Welsch, B. T. 2007, *ApJ*, 666, 576, doi: [10.1086/518994](https://doi.org/10.1086/518994)
- Demoulin, P., Henoux, J. C., Priest, E. R., & Mandrini, C. H. 1996, *A&A*, 308, 643
- Deng, N., Chen, X., Liu, C., et al. 2015, *ApJ*, 799, 219, doi: [10.1088/0004-637X/799/2/219](https://doi.org/10.1088/0004-637X/799/2/219)
- Goode, P. R., Coulter, R., Gorceix, N., Yurchyshyn, V., & Cao, W. 2010a, *Astronomische Nachrichten*, 331, 620, doi: [10.1002/asna.201011387](https://doi.org/10.1002/asna.201011387)
- Goode, P. R., Yurchyshyn, V., Cao, W., et al. 2010b, *ApJL*, 714, L31, doi: [10.1088/2041-8205/714/1/L31](https://doi.org/10.1088/2041-8205/714/1/L31)
- Kuridze, D., Henriques, V., Mathioudakis, M., et al. 2015, *ApJ*, 802, 26, doi: [10.1088/0004-637X/802/1/26](https://doi.org/10.1088/0004-637X/802/1/26)
- Langangen, Ø., De Pontieu, B., Carlsson, M., et al. 2008, *ApJL*, 679, L167, doi: [10.1086/589442](https://doi.org/10.1086/589442)
- Liu, J., Nelson, C., Snow, B., Wang, Y., & Erdélyi, R. 2019, *Nature Communications*, 10, doi: [10.1038/s41467-019-11495-0](https://doi.org/10.1038/s41467-019-11495-0)
- Liu, R., Kliem, B., Titov, V. S., et al. 2016, *ApJ*, 818, 148, doi: [10.3847/0004-637X/818/2/148](https://doi.org/10.3847/0004-637X/818/2/148)
- Martínez-Sykora, J., De Pontieu, B., De Moortel, I., Hansteen, V. H., & Carlsson, M. 2018, *ApJ*, 860, 116, doi: [10.3847/1538-4357/aac2ca](https://doi.org/10.3847/1538-4357/aac2ca)
- Martínez-Sykora, J., De Pontieu, B., Hansteen, V. H., et al. 2017, *Science*, 356, 1269, doi: [10.1126/science.aah5412](https://doi.org/10.1126/science.aah5412)
- Mason, E. I., Antiochos, S. K., & Bradshaw, S. 2023, *ApJ*, 943, 84, doi: [10.3847/1538-4357/acac85](https://doi.org/10.3847/1538-4357/acac85)
- McIntosh, S. W., De Pontieu, B., Carlsson, M., et al. 2011, *Nature*, 475, 477, doi: [10.1038/nature10235](https://doi.org/10.1038/nature10235)
- McLaughlin, J. A., Verth, G., Fedun, V., & Erdélyi, R. 2012, *ApJ*, 749, 30, doi: [10.1088/0004-637X/749/1/30](https://doi.org/10.1088/0004-637X/749/1/30)

- Metcalf, T. R., Leka, K. D., Barnes, G., et al. 2006, *SoPh*, 237, 267, doi: [10.1007/s11207-006-0170-x](https://doi.org/10.1007/s11207-006-0170-x)
- Narang, N., Arbacher, R. T., Tian, H., et al. 2016, *SoPh*, 291, 1129, doi: [10.1007/s11207-016-0886-1](https://doi.org/10.1007/s11207-016-0886-1)
- Okamoto, T. J., & De Pontieu, B. 2011, *ApJL*, 736, L24, doi: [10.1088/2041-8205/736/2/L24](https://doi.org/10.1088/2041-8205/736/2/L24)
- Pereira, T. M. D., Rouppe van der Voort, L., & Carlsson, M. 2016, *ApJ*, 824, 65, doi: [10.3847/0004-637X/824/2/65](https://doi.org/10.3847/0004-637X/824/2/65)
- Pereira, T. M. D., De Pontieu, B., Carlsson, M., et al. 2014, *ApJL*, 792, L15, doi: [10.1088/2041-8205/792/1/L15](https://doi.org/10.1088/2041-8205/792/1/L15)
- Rouppe van der Voort, L., Leenaarts, J., De Pontieu, B., Carlsson, M., & Vissers, G. 2009, *ApJ*, 705, 272, doi: [10.1088/0004-637X/705/1/272](https://doi.org/10.1088/0004-637X/705/1/272)
- Rutten, R. J. 2006, in *Astronomical Society of the Pacific Conference Series*, Vol. 354, *Solar MHD Theory and Observations: A High Spatial Resolution Perspective*, ed. J. Leibacher, R. F. Stein, & H. Uitenbroek, 276. <https://arxiv.org/abs/astro-ph/0701379>
- Samanta, T., Tian, H., Yurchyshyn, V., et al. 2019, *Science*, 366, 890, doi: [10.1126/science.aaw2796](https://doi.org/10.1126/science.aaw2796)
- Scherrer, P. H., Schou, J., Bush, R. I., et al. 2012, *SoPh*, 275, 207, doi: [10.1007/s11207-011-9834-2](https://doi.org/10.1007/s11207-011-9834-2)
- Schou, J., Scherrer, P. H., Bush, R. I., et al. 2012, *SoPh*, 275, 229, doi: [10.1007/s11207-011-9842-2](https://doi.org/10.1007/s11207-011-9842-2)
- Sekse, D. H., Rouppe van der Voort, L., & De Pontieu, B. 2013, *ApJ*, 764, 164, doi: [10.1088/0004-637X/764/2/164](https://doi.org/10.1088/0004-637X/764/2/164)
- Sterling, A. C., Moore, R. L., Samanta, T., & Yurchyshyn, V. 2020, *ApJL*, 893, L45, doi: [10.3847/2041-8213/ab86a5](https://doi.org/10.3847/2041-8213/ab86a5)
- Suematsu, Y., Ichimoto, K., Katsukawa, Y., et al. 2008, in *Astronomical Society of the Pacific Conference Series*, Vol. 397, *First Results From Hinode*, ed. S. A. Matthews, J. M. Davis, & L. K. Harra, 27
- Tian, H., DeLuca, E. E., Cranmer, S. R., et al. 2014, *Science*, 346, 1255711, doi: [10.1126/science.1255711](https://doi.org/10.1126/science.1255711)
- Titov, V. S. 2007, *ApJ*, 660, 863, doi: [10.1086/512671](https://doi.org/10.1086/512671)
- Titov, V. S., Hornig, G., & Démoulin, P. 2002, *Journal of Geophysical Research (Space Physics)*, 107, 1164, doi: [10.1029/2001JA000278](https://doi.org/10.1029/2001JA000278)
- Tomczyk, S., McIntosh, S. W., Keil, S. L., et al. 2007, *Science*, 317, 1192, doi: [10.1126/science.1143304](https://doi.org/10.1126/science.1143304)
- van Ballegooijen, A. A., Asgari-Targhi, M., Cranmer, S. R., & DeLuca, E. E. 2011, *ApJ*, 736, 3, doi: [10.1088/0004-637X/736/1/3](https://doi.org/10.1088/0004-637X/736/1/3)
- Vilangot Nhalil, N., Shetye, J., & Doyle, J. G. 2023, *MNRAS*, 524, 1156, doi: [10.1093/mnras/stad1742](https://doi.org/10.1093/mnras/stad1742)
- Wang, J., Lee, J., Liu, C., Cao, W., & Wang, H. 2022, *ApJ*, 924, 137, doi: [10.3847/1538-4357/ac374e](https://doi.org/10.3847/1538-4357/ac374e)
- Wöger, F., & von der Lühe, O. 2007, *Appl. Opt.*, 46, 8015
- Yurchyshyn, V., Abramenko, V., & Goode, P. 2013, *ApJ*, 767, 17, doi: [10.1088/0004-637X/767/1/17](https://doi.org/10.1088/0004-637X/767/1/17)
- Yurchyshyn, V., Cao, W., Abramenko, V., Yang, X., & Cho, K.-S. 2020, *ApJL*, 891, L21, doi: [10.3847/2041-8213/ab7931](https://doi.org/10.3847/2041-8213/ab7931)